Title

Coastal Stratocumulus cloud edge forecasts

Authors

Wu, Elynn
Clemesha, Rachel ES
Kleissl, Jan

Publication Date

2018-04-01

DOI

10.1016/j.solener.2018.02.072

Peer reviewed

Title: **Coastal Stratocumulus cloud edge forecasts**

Authors: Elynn Wu[a,*] (corresponding author), Rachel E. S. Clemesha[b], Jan Kleissl[a]
[a]Center for Renewable Resources and Integration, Department of Mechanical and Aerospace Engineering, University of California, San Diego, 9500 Gilman Drive, La Jolla, CA 92093-0411, USA.
[b]Scripps Institution of Oceanography, University of California, San Diego, 9500 Gilman Drive, La Jolla, CA 92093-0230, USA.
Email: elw014@eng.ucsd.edu

Abstract

Improved coastal Stratocumulus (Sc) cloud forecasts are needed because traditional satellite cloud motion vectors (CMV) do not accurately predict how Sc clouds move or dissipate in time, which often results in underprediction of irradiance in the morning hours. CMV forecasts assume clouds to move in the direction of the average regional wind field, which is not necessarily the case for Sc. Sc clouds over the land form at night and typically reach maximum coverage before sunrise. During the day, heating from solar radiation at the surface and entrainment of dry and warm air from above causes Sc clouds to dissipate. A Sc cloud edge forecast using Geostationary Operational Environmental Satellite is proposed to improve the Sc cloud dissipation forecast during the day. The inland edge of Sc clouds is tracked in time and extrapolated into the future. In coastal California, the Sc inland boundary is correlated to the land elevation. Dissipation after sunrise often follows land elevation as the amount of air required to be heated to become cloud-free decreases with increasing elevation since cloud top height is fairly constant along the cloud edge. The correlation between land elevation and Sc eastern boundary is exploited by extrapolating the evolution of cloud edge elevation in time. This method is tested in central and northern California on 25 days and in southern California on 19 days. When compared to the CMV and persistence forecasts, the proposed Sc cloud edge forecasts show a reduction of 30 Wm^{-2} and 107 Wm^{-2} in hourly mean absolute error (MAE) of global horizontal irradiance. Additionally, out of 11 stations the line forecast results show a higher forecast skill than CMV (persistent) at 7 (9) stations.

1. Introduction

Sc clouds are the most common cloud type on Earth, with an annual mean coverage of 22% for the ocean surface and 12% for the land surface (Hahn and Warren, 2007). Sc clouds strongly reflect incoming solar radiation. Since they emit a similar amount of outgoing longwave radiation as the surface due to their low cloud height, Sc clouds have a strong net negative radiative effect on the Earth radiative balance (Hartmann et al., 1992; Wood, 2012). Sc clouds form in a shallow planetary boundary layer and are capped by a strong temperature inversion. The inversion limits the vertical mixing of warm dry air above and cool moist air beneath (Klein and Hartmann, 1993), which keeps the clouds from evaporating. Geographically, the highest Sc land coverage is found in the mid-latitude coastal region next to eastern boundary currents (Wood, 2012), and the temperature inversion in this region is associated with the warm dry descending branch of the Hadley cell.

Coastal California is an area of high Sc cloud coverage during the late spring and summer months when the semi-permanent North Pacific High has the greatest intensity (Clemesha et al., 2016). Sc clouds greatly influence the weather, water, and energy of the ecosystem and have been a topic of extensive research for many years (Beer and Leopold, 1947; Iacobellis and Cayan, 2013; Johnstone and Dawson, 2010; Williams et al., 2015). In recent years, an aggressive renewable energy mandate in the state of California has attracted more than half a million rooftop solar photovoltaic (PV) installations. As solar PV

becomes an important source of generation to the grid, it is critical for the utilities and system operators to maintain reliable service while maximizing solar energy utilization (Denholm et al., 2016). With a majority of rooftop solar PV along the densely-populated coast of California, an accurate forecast of Sc clouds during the summer months becomes important as these clouds reduce solar irradiance substantially.

Two types of methods are used in solar irradiance forecasting depending on the forecast horizon. For short-term solar forecasting, imagery-based cloud advection is used. Ground-based sky imager systems are used for intra-hour forecasting (Chow et al., 2011; Huang et al., 2013; Yang et al., 2014; Peng et al., 2015), while satellite cloud motion vectors (CMV) are used for forecasting up to 5-hour ahead (Perez et al., 2010). Traditional image-based cloud advection assumes "frozen" clouds to move in the direction of the regional wind field. While this assumption generally holds true for a few hours, it loses validity for longer term forecast. For longer-term solar forecasting, ranging from hours-ahead to days-ahead, physics-based numerical weather prediction (NWP) is used (Jimenez et al., 2016; Lara-Fanego et al., 2012; Mathiesen and Kleissl, 2011). NWP uses current weather observations to solve a set of primitive equations and numerically integrate the weather forward in time. Forecast accuracy varies considerably depending on the time, location, and weather condition. Perez et al. (2010) found that hourly-averaged satellite CMV forecast mean bias error (MBE) and root mean square error (RMSE) range from 0.2 W m^{-2} and 104 Wm^{-2} in an arid region like Desert Rock, NV to 30 Wm^{-2} and 159 Wm^{-2} in a semi-arid elevated place like Boulder, CO on an annual basis. Mathiesen and Kleissl (2011) found that NWP models generally under-predict cloudy conditions, resulting in an over-prediction of solar irradiance. Recent studies have combined satellite images and NWP to better improve short-term solar forecasting (Arbizu-Barrena et al., 2017; Lee et al., 2017). For example, in addition to using traditional CMV techniques, Arbizu-Barrena et al. (2017) uses a NWP to allow both advection and diffusion to the cloud index derived from Meteosat Second Generation. It is shown that this technique outperforms traditional CMV in areas with low topographic complexity but struggles in areas where cloud patterns are influenced by the terrain.

NWP forecasts of Sc clouds in coastal California have been improved through better cloud initialization (Mathiesen et al., 2013; Yang and Kleissl, 2016) or modifying inversion base height in NWP to better represent the clouds (Zhong et al., 2017). Imagery-based cloud advection forecasts have received less attention. Traditional satellite CMV forecasts do not accurately predict how Sc clouds move or dissipate in time largely because Sc clouds do not typically follow the synoptic wind direction. Sc clouds over land often form at night and reach maximum coverage before sunrise. During the day, Sc clouds dissipate because of solar heating at the surface (and the resulting surface sensible heat flux), solar heating of the cloud, and entrainment of drier warmer air from aloft (Ghonima et al., 2016). Since dissipation of Sc clouds is not considered, frozen cloud advection in satellite CMV often under-predicts solar irradiance.

The objective of this paper is to improve solar irradiance forecasting during Sc days primarily through quantifying the dissipation time of Sc clouds. A Sc cloud edge forecast (hereinafter called "line forecast") using the Geostationary Operational Environmental Satellite (GOES) is proposed to improve the cloud dissipation forecast during the day. The forecast is based on tracking the most inland edge of Sc clouds. The novelty of the method is that it can track evolution (dissipation in this case) of a stationary cloud, while standard cloud motion approaches only consider advection of frozen clouds. The method combines physical insights into lower atmospheric cloud top heights under a strong inversion with statistical methods. While applied here to Sc forecasting in California, we expect the cloud edge tracking to be equally valid for other overcast stationary clouds such as coastal Sc forecasts elsewhere and inland fog forecasts. For example, fog and low stratus in Germany pose a challenge for the transmission system operators. In addition to the low stratus risk forecast system designed for day-ahead warnings (Köhler et al. 2017), line forecasts for short-term forecasting could also help support the decision makings.

This paper is organized as follows. Section 2 explains the conceptual motivation and assumptions of the line forecast (2.1), followed by a description of Sc cloud dissipation time and cloud thickness evolution (2.2 and 2.3). Then error metrics is presented in (2.4). Section 3 contains input data (3.1 and 3.2), case study setup (3.3, and validation sites and data (1.1). Section 1 contains the validation results and discussion. Validation of assumptions are investigated in 4.1, followed by validation against satellite observations (4.2) and discussion of geographical error distributions (4.3). Finally, Section 5 provides conclusions.

2. Methods

2.1 Cloud edge line forecast – conceptual motivation and assumptions

In coastal California, the Sc eastern (inland) boundary edge elevation is typically found to be at a maximum during the early morning and then decreases in time. Conceptually, clouds thicken and spread at night due to longwave cooling, but start to thin when longwave radiative cooling is balanced by solar heating, which occurs shortly after sunrise (Akyurek and Kleissl, 2017). In southern California, the terrain rises nearly monotonically and peaks at about 1.5 km elevation 40 to 80 km inland. The eastern boundary of Sc clouds usually follows isolines of land elevation. Iacobellis and Cayan (2013) showed that the inland penetration of Sc clouds is limited by the height of the inversion base and coastal topography. In other words, Sc clouds extend inland up to where the land elevation reaches the inversion base height, and the inversion base height equals the cloud top height. Dissipation of Sc clouds occurs after sunrise, often following land elevation as the amount of air required to be heated to become cloud-free decreases with increasing elevation.

The line forecast employs the correlation between land elevation and Sc eastern boundary, by extrapolating the evolution of cloud edge elevation in time to predict future cloud edge location. The line forecasts assume: (i) constant inversion height (and cloud top height) along the cloud edge; (ii) a constant rate of decrease in the cloud edge boundary elevation, (iii) an exponential increase in normalized global horizontal irradiance (clear sky index) from sunrise to one when the clouds dissipate, and (iv) no satellite parallax effect. Assumptions (ii) and (iii) will be tested in Section 4.1. Rastogi et al. (2016) investigated the inversion base height at San Diego Miramar (NKX: 32.85^{o}N, 117.11^{o}W), Vandenberg Air Force Base (VBG: 34.75^{o}N, 120.56^{o}W), and the northern Channel Islands (approximately 33.97^{o}N, 119.85^{o}N) during 1965—2015 using radiosonde data and the Modern-Era Retrospective Analysis for Research and Applications (MERRA)(Rienecker et al., 2011). While radiosonde data showed that inversion height is generally 100 m lower at VBG than NKX, MERRA data showed nearly identical inversion base height for the three points. Although radiosonde data showed differences between VBG and NKX, the lack of spatial coverage made it hard to determine the inversion height everywhere in the domain. As such, assumption (i) was treated as valid for this study. Since the GOES satellite is at a zenith angle of approximately 43 degrees and 50 degrees in the southern and northern end of California, the projection of the cloud edge on the surface will be displaced horizontally by tan (zenith angle) times cloud top height above ground level. However, since average cloud top heights are only 400 m above mean sea level the parallax error is small relatively to the scales of terrain elevation changes and the horizontal resolution of the satellite images.

2.2 Cloud Dissipation Time

The GOES visible channel captures a new image every 15-minutes. At each time step of satellite image, a visible reflectance cloud test (Iacobellis and Cayan, 2013) is performed, and the eastern boundary of Sc clouds with its corresponding land elevation are extracted. The median land elevation of the boundary is

used to represent the elevation at each time step. Any missing time steps are ignored. The time stamp of the line forecast model is every 15-minute. An example of the Sc inland boundary moving towards lower land elevation is shown in Figure 1. The median land elevation of the boundary as shown in Figure 1 decreases from 900 m at 0700 to 370 m at 1000 PST. Pacific Standard Time (PST) lags Coordinated Universal Time (UTC) by 8 hours and would be used for the remainder of this study. Figure 2 shows the step by step approach to issue a Sc line forecast for this day. A time series of the boundary median elevation is shown in Figure 2b.

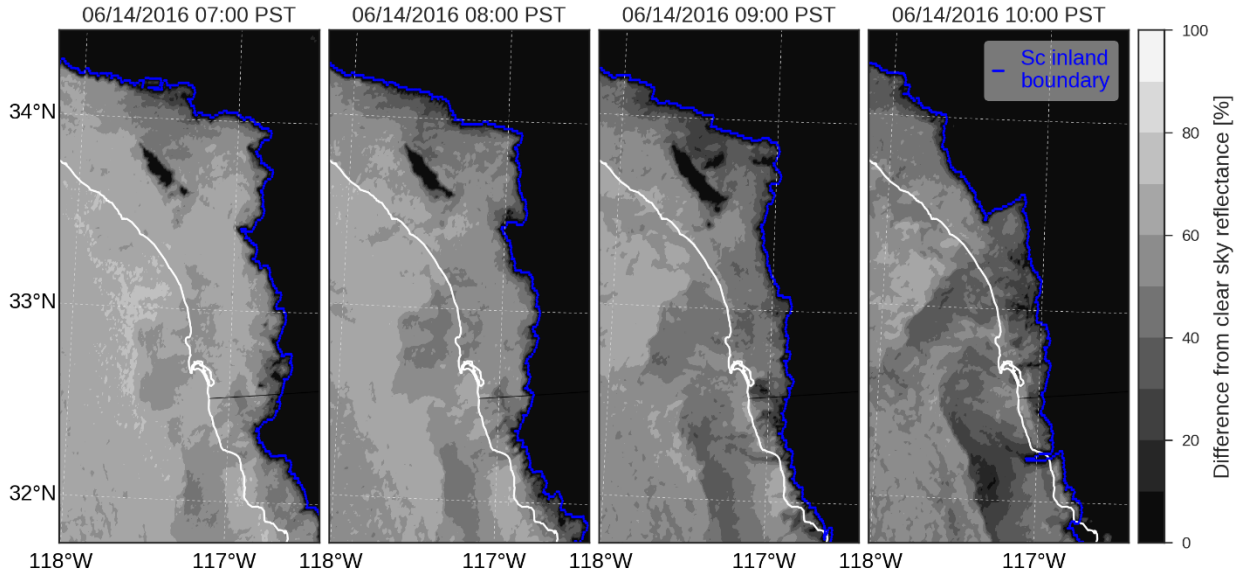

Figure 1. GOES visible images at 0700, 0800, 0900, and 1000 PST on June 14, 2016 with Sc inland boundary highlighted. Raw images are post-processed such that pixels within 15.5% of their clear sky reflectance are plotted as dark (clear), while pixels with larger than 15.5% difference are plotted in grey scales (cloudy). Threshold value of 15.5% was previously tested and optimized (See Text S1 in Clemesha et al. (2016)). The position of the boundary advances towards the coast from 0700 to 1000 PST. Note that Santa Ana Mountains (33.7^{o}N, 117.5^{o}W) are clear because the land elevation is above the inversion base height.

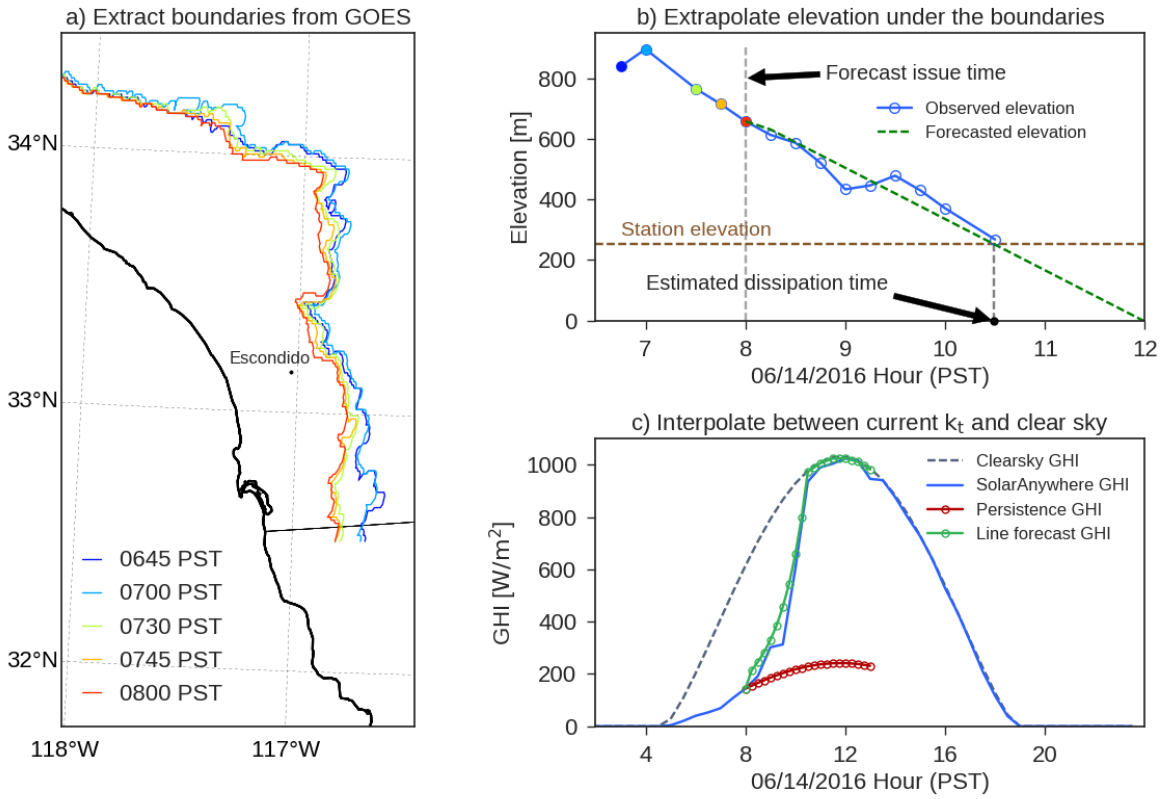

Figure 2. Steps to issue a cloud edge or the line forecast at 0800 PST for Escondido with a land elevation of 250 m: (a) Extract Sc inland boundary in consecutive GOES images up to 0800 PST and record the median land elevation under the colored lines (between 32.5°N and 34.5°N). (b) Extrapolate median land elevation in time using a best fit line through 0645 to 0800 PST. Cloud dissipation time is when the forecasted elevation intercepts with the station elevation (approximately 1030 PST). (c) Interpolate between current k_t at 0800 PST and clear sky k_t at cloud dissipation time using the exponential function described in Section 4.1. The green line in (c) is the line forecast issued at 0800 PST with a 15-minute time resolution. Note that the accuracy of the line forecast is limited by the number of visible images available. While the forecast issued at 0800 PST showed great results for this day, the line forecast would not be able to accurately predict the cloud dissipation time for the forecast issued at 0700 PST. As seen in (b), only two elevation points were available at 0700 PST, and the extrapolation of median land elevation would result in clouds persisting for the whole day.

To predict when Sc clouds will dissipate at a given location, a linear regression is performed on a time series of the points corresponding to Sc eastern boundary land elevation (Figure 2b) and extrapolated in time to the elevation for the given location. A linear regression is chosen based on observation, and the assumption will be tested in the next section. The method uses a least square linear fit . It is hypothesized that the time when the predicted elevation reaches the elevation of the specified location is the time when Sc clouds dissipate:

$$t_{clear} = \frac{E_{site} - a}{b}, \quad (1)$$

where E_{site} is the land elevation of the site of interest, and a and b are the intercept and slope from the least square linear fit.

2.3 Cloud Thickness Evolution

To describe the cloud thickness evolution between forecast issue time and dissipation time, the normalized global horizontal irradiance (clear-sky index, k_t) is interpolated using an exponential function between forecast issue time and dissipation time to represent the thinning of Sc clouds:

$$k_t{}^*(t^*) = ae^{bt^*} + c\,, \tag{2}$$

where a, b, and c are constant coefficients. $k_t{}^*$ and t^* are normalized k_t and time stamp, and the equations are shown later in Eq. (3) and (4). Physically, when the sun angle is low (early morning), not much heat is received at the surface and the thickness of the clouds is approximately constant. As the day progresses, solar heating increases drastically, and the cloud thickness decreases successively quicker. As such, the exponential function is chosen.

The clear sky irradiance model from Perez et al. (2002) is used to compute k_t. To determine the coefficients for the fitted exponential function, the coastal low cloudiness dataset from Clemesha et al. (2016) is used. The dataset was created using GOES images from 1996 to 2016 with a spatial resolution of 4 km and a temporal resolution of 30-minute. Historical days within the dataset when Sc clouds are present are identified. The corresponding SolarAnywhere (2017) data, a satellite solar irradiance product, are extracted to determine the exponential function that best describes the increase in k_t from sunrise to cloud dissipation time. SolarAnywhere data are available from 2003 to 2016, and only the overlapped time period between coastal low cloudiness dataset and SolarAnywhere are used. Note that 2016 is excluded in this analysis as it will be used to validate the forecast. June and August are selected as they represent the months with most dominant marine layer cloud influence in southern and northern California, respectively. A map of southern and central and northern California domain is shown in Figure 3.

Time stamps are scaled by the time difference between sunrise and cloud dissipation time:

$$t^* = \frac{t - t_{sunrise}}{t_{clear,obs} - t_{sunrise}}, \text{for } t_{sunrise} \le t \le t_{clear,obs}\,, \tag{3}$$

where $t_{clear,obs}$ is the first time when observed k_t is clear, and $t_{sunrise}$ is the time stamp at sunrise. The observed clear k_t is defined following Kankiewicz et al.(2014) where clear sky is defined as k_t greater than 0.8. Sunrise is chosen as the reference time since that is when solar heating starts to thin the cloud deck. Similarly, to normalize different starting k_t at sunrise, k_t for each individual day is scaled by k_t at sunrise:

$$k_t^* = \frac{k_t - k_{t_{sunrise}}}{1 - k_{t_{sunrise}}}, \tag{4}$$

where $k_{t_{sunrise}}$ is the clear sky index at sunrise. To avoid picking earlier points where the accuracy of k_t decreases because of difficulty of modeling clear sky irradiance near sunrise, the first daytime point is chosen to be when cosine of solar zenith angle is greater than 0.1. Cosine of solar zenith angles are calculated for all stations shown in Figure 3. During the month of June, 0530 PST marks the time when cos (solar zenith angle) is greater than 0.1 for stations in southern California. For central and northern California, 0600 PST marks the time when the criteria are met for early August while gradually shifting to 0630 PST for late August.

An example of the fitted exponential function at a single site is shown in Figure 4. For this study, two sets of coefficients are determined after repeating the analysis for multiple sites. The first set will be used to forecast k_t in central and northern California in August, and the second set will be used to forecast k_t in southern California in June. The coefficients are tabulated in Table 1 and the corresponding curves can

be seen in Figure 5. The exponential growth rate is slightly higher in central and northern California (larger b in Eq. (2)), while the initial k_t is slightly higher in southern California (larger a in Eq. (2)). The stations shown in this analysis will be used as validation sites and will be discussed in greater details in Section 3.4.1.

To produce a time series of forecasted k_t, forecast issue time and future time stamps are scaled following Eq. (3), and cloud dissipation time is calculated following Eq. (1). These scaled time stamps are then plugged into Eq. (2) to retrieve k_t^*. Lastly, k_t^* is transformed back to k_t by rearranging Eq. (4) and replacing $k_{t_{sunrise}}$ as k_t at forecast issue time t_o:

$$k_t = k_t^*\left(1 - k_{t,0}\right) + k_{t,0}\,. \tag{5}$$

This k_t model has the benefit that points that are falsely flagged as cloudy by the line forecast at the forecast issue time (e.g. land elevation is lower than the median land elevation of the boundary yet the pixel is initially clear), are automatically corrected to clear because future k_t is an interpolation between current k_t ($k_{t,0} = 1$ in this case) and clear k_t (i.e. $k_t = 1$). In other words, these points will not be changed to lower k_t and will remain clear.

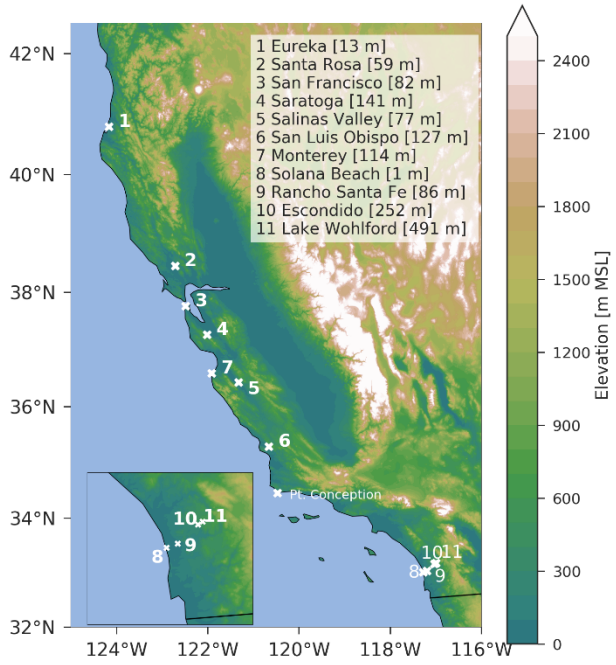

Figure 3: Map of elevation and validation sites. Specific site elevation is given in the legend. The cut-off for southern California and central and northern California is around Pt. Conception, all southern California stations are shown in the inset.

208

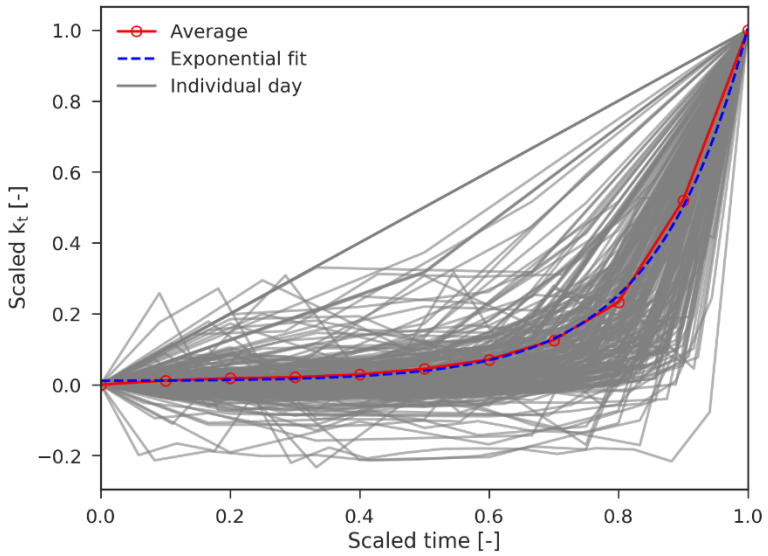

209

Figure 4. Scaled time t^* and scaled clear sky index k_t^* for Sc cloud days in August from 2003 to 2015 at Santa Rosa, CA. The average of the k_t^* for individual days (red line) are used to fit the exponential function (blue line). Negative k_t^* during the day indicates a decrease of k_t from sunrise.

Table 1 Coefficients of the average of the fitted exponential function in Eq. (2) for central and northern California and southern California (black dashed lines in Figure 5) for different sunrise time.

Location	a	b	c
Central and northern California (sunrise at 0600 PST)	0.003	5.959	0.022
Central and northern California (sunrise at 0630 PST)	0.006	5.041	0.022
Southern California (sunrise at 0530 PST)	0.005	5.238	0.014

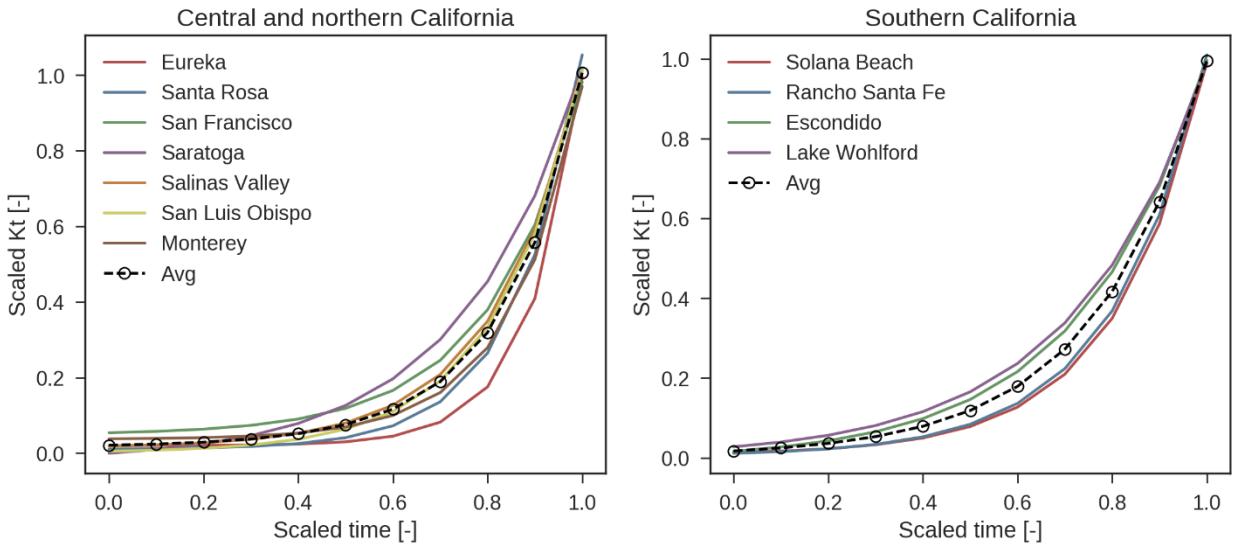

Figure 5. The fitted exponential function at each individual station and their average for central and northern (left) and southern California (right). The corresponding coefficients can be found in Table 1.

2.4 Error metrics

The error metrics used for validation are mean bias error (MBE), mean absolute error (MAE), and forecast skill (FS):

$$MBE \equiv \frac{1}{N}\sum_{n=1}^{N} x_n - {x_n}^{obs} \tag{6}$$

$$MAE \equiv \frac{1}{N}\sum_{n=1}^{N} \left| x_n - {x_n}^{obs} \right| \tag{7}$$

$$FS \equiv 1 - \frac{MAE}{MAE_{persistence}}, \tag{8}$$

where x_n is the nth forecast GHI, and ${x_n}^{obs}$ is the nth observation GHI. To further quantify the skill of Sc line forecast, the FS defined by Coimbra et al. (2013) and modified by Yang and Kleissl (2016) is used to intercompare line forecasts against persistence forecasts. Positive values of FS indicate that line forecasts have a lower MAE than persistence forecasts. The maximum value of FS is 1.

3. Data and Validation

3.1 Elevation data

Land elevation data are obtained from General Bathymetric Chart of the Oceans (GEBCO, 2017) at 30 arc-second intervals (or approximately 1 km). At each time stamp, the land elevation at the cloud boundary is retrieved. Land points below the median cloud boundary elevation are assumed to be cloudy, and the median cloud boundary land elevation is assumed to be decreasing during the day. In other words, non-negative slope *b* in Eq. (1) are not considered, but such cases are limited to early

morning, presumably because solar heating is still weaker than longwave cooling at large solar zenith angles, leading to initial increase in cloud cover and/or thickness (Akyurek and Kleissl, 2017). On most days, the elevation eventually drops to sea level, representing a complete clearing of Sc clouds for the coastal land area. Cloud boundaries over the ocean are ignored as the focus of this paper is solar irradiance forecast over the land.

Further constraints on the domain are required to avoid assigning far inland points as cloudy because they have a land elevation below the median Sc cloud edge elevation. The topography of coastal California rises steeply near the coast, but then drops to near sea level across the coastal mountain range in the Central Valley and Imperial Valley. In reality, Sc clouds seldom penetrate that far inland as the mountain ranges act as barriers to the airmasses that support Sc clouds. The inland valleys represent arid climates and are mostly clear throughout the summer. To constrain the domain to areas where Sc clouds commonly occur, we filter the points using the 20 year summertime California coastal low cloudiness dataset from Clemesha et al. (2016). Land points with no low cloud occurrence in the 20-year low cloud dataset are removed from the cloud mask. Doing so also assures that the extrapolation of boundary elevation will not include land points with the same land elevation but too far inland (e.g. a land point can be at sea level but located a few hundred kilometers away from the coast). The final coastal domain is can be seen in Figure *6*.

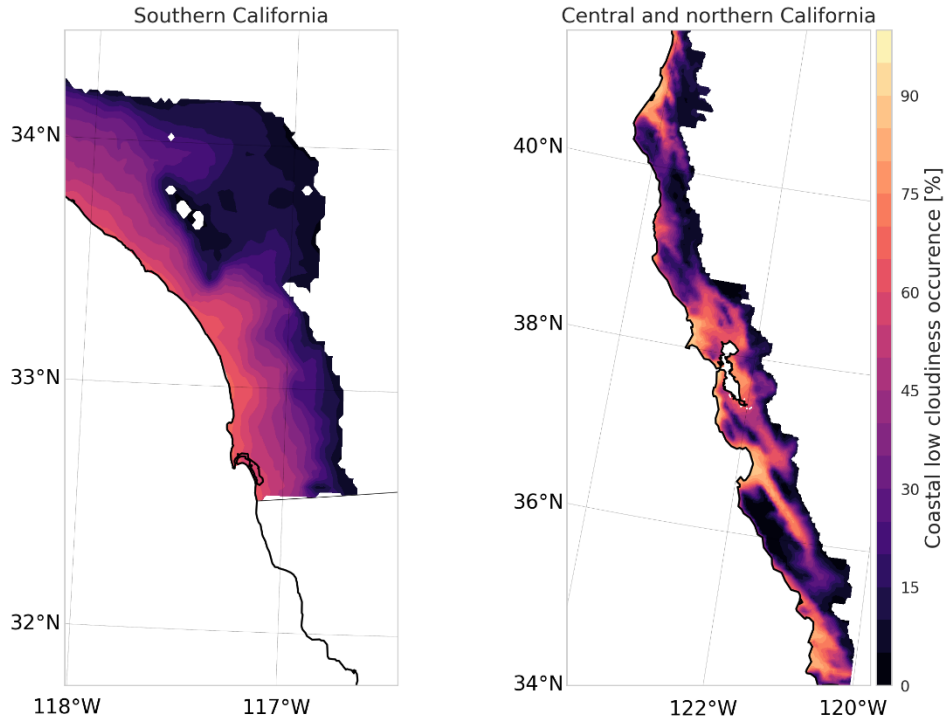

Figure 6. California coastal low cloudiness (Clemesha et al., 2016) occurrence is averaged between 0600 to 0800 PST over 20-year for June in southern California and August for central and northern California.

3.2 GOES data and cloud edge retrieval

GOES-15 Imager measurements in the visible channel at 1 km resolution are obtained from National Oceanic and Atmospheric Administration (NOAA) Comprehensive Large Array-Data Stewardship System (CLASS). Images are captured every 15 minutes. During the daytime hours, images are missing at 1515,

1015, 1245, and 1315 PST. A post-launch calibration developed at NOAA's National Environmental Satellite, Data, and Information Services (NESDIS, 2017) is applied to the images to account for sensor degradation.

To retrieve clouds from the satellite images, a clear sky or background reflectance is determined by sorting the reflectance from all images at each month and hour and selecting the minimum reflectance at each pixel (Iacobellis and Cayan, 2013). Instead of using the preceding one month of data (~30 images) as was the case in Iacobellis and Cayan (2013), we use the preceding three months of data (~90 images) because it yields a better cloud detection. This method assumes that there is at least one clear day during the three-month window. After obtaining clear sky reflectance for every pixel, a binary cloud mask is turned on every time the pixel reflectance exceeds its clear sky reflectance by 15.5% (Clemesha et al., 2016). Once the cloud mask at each time stamp is determined, the longest consecutive contour line is extracted as the Sc eastern boundary.

3.3 Location and time period for the case studies

As mentioned in Section 2.3, June and August are the peak months of southern and northern California coastal low clouds. Therefore, the month of June and August 2016 are chosen for southern California and central and northern California for validation, respectively. We quantify days with Sc cloud coverage using the following approach: (1) For the first visible image of the day, at least 10 % of cloud coverage in the coastal low cloudiness product are present over land in each domain. (2) Use the corresponding thermal infrared image at 10.7 µm to compute scene temperature (i.e. cloud top temperature) following Weinreb and Han (2011). Since Sc clouds are low and have relatively uniform cloud top height, the variation in cloud top temperature in the coastal domain is used to exclude days with significant amount of high clouds. After threshold testing, a standard deviation in cloud temperature of 3 % (about 8 K) among the cloudy pixels is chosen. Days with scene temperature standard deviation greater than 3 % are removed. While the standard deviation thresholding removes days with significant multi-level clouds (i.e. both low and high clouds are in the domain), there are some days when the proportion of high clouds is too small to raise the standard deviation above 3%. These days are kept in the dataset, but to avoid misclassifying the cloud edge elevation, land elevation at pixels with scene temperature lower than 280 K are removed. A flowchart of when the line forecast should be used is shown in Figure *7*.

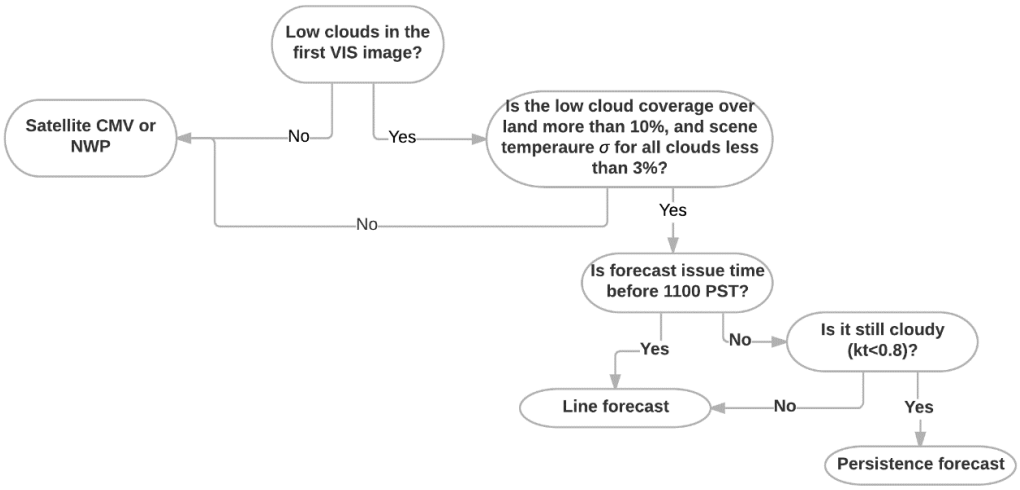

Figure 7. Flowchart of line forecast criteria.

For southern California, a total of 19 days passed (June 1 to 9, 11 to 15, 23 to 25, and 29 to 30) the threshold tests. For central and northern California, a total of 25 days passed (August 1 to 28, excluding August 18, 19, and 22).

3.4 Validation

3.4.1 Validation sites

For the central and northern California case study, seven cities ranging from as far north as Eureka to as far south as San Luis Obispo are chosen as validation sites. Their locations and elevations are tabulated in Table 2. The sites are carefully chosen to represent the different challenges in forecasting Sc clouds in different regions.

For the southern California case study with a focus in the greater San Diego area, four sites along a line from coastal to inland are chosen. These four sites are part of the San Diego Gas & Electric (SDGE) weather station network with LI-COR LI200 pyranometers measuring global horizontal irradiance (GHI) at 5-minute resolution. Their locations and elevations are tabulated in Table 3. A map of all 11 validation sites is shown earlier in Figure 3.

Table 2
Summary of validation sites in central and northern California. Median Sc burn-off time is obtained from 20 August months (1996 — 2015) using the coastal low cloudiness product at half hour time resolution.

Station	Eureka	Santa Rosa	San Francisco	Saratoga	Salinas Valley	San Luis Obispo	Monterey
Latitude [^{o}]	40.798	38.447	37.752	37.262	36.427	35.283	36.583
Longitude [^{o}]	-124.163	-122.709	-122.477	-122.013	-121.322	-120.653	-121.906
Elevation [m MSL]	13	59	82	141	77	127	114
Median Sc burn-off time [HHMM PST]	1130	0930	1230	0800	0900	0830	1130

Table 3
Summary of validation sites in southern California. Median Sc burn-off time is obtained from 20 June months (1996 — 2015) using the coastal low cloudiness product at half hour time resolution.

Station	Solana Beach	Rancho Santa Fe	Escondido	Lake Wohlford
Latitude [^{o}]	33.007	33.033	33.159	33.178
Longitude [^{o}]	-117.276	-117.189	-117.031	-116.995
Elevation [m MSL]	1	86	252	491

Median Sc burn-off time [HHMM PST]	0900	0830	0800	0800

3.4.2 Satellite solar resource data

Clean Power Research's SolarAnywhere (2017) data utilizes GOES images to output solar irradiance by modulating a clear sky irradiance model (Perez et al., 2002). For June 2016, SolarAnywhere data are validated against the SDGE weather stations, with an average hourly MBE of 18 W m^{-2}, MAE of 30 W m^{-2}, and RMSE of 57 W m^{-2}. Jamaly and Kleissl (2012) also validated SolarAnywhere data against 52 California Irrigation Management Information System (CIMIS) ground sensors and found similar results— an average hourly MBE of 19 W m^{-2}, MAE of 46 W m^{-2}, and RMSE of 65 W m^{-2} over the year 2010. Since the accuracy is comparable to that of a typical ground sensor, accurate under typical conditions to ±5 % (CIMIS, n.d.), SolarAnywhere data will be used as observations for validation hereinafter. SolarAnywhere data at 2 km spatial resolution and 30-minute temporal resolution are retrieved for the 11 validation sites.

3.4.3 Satellite cloud motion vector and persistence forecast

For reference, hourly satellite CMV data (Perez et al., 2010) from 1-hour to 5-hour ahead derived from GOES images are computed for the 11 validation sites. For the 7 sites in central and northern California, data are available for 1—31 August 2016. For the 4 sites in southern California, data are only available for 5—15 June 2016. The (smart) persistence forecast uses the clear sky index (k_t) from SolarAnywhere satellite measurements at forecast issue time and assumes fixed k_t out to 5-hour ahead.

4. Results and Discussion

4.1 Validation of assumptions

Two assumptions described in Section 2.1 are tested here. If the Sc boundary elevation decreases at a constant rate, then a linear least-square regression through the elevation points should have a coefficient of determination (r^2) that is close to 1. For each validation day, boundary elevation derived from GOES images between 0630 to 1230 PST (~23 images) as shown in Figure 8 are used to fit a linear least-square regression, and the r^2 is recorded. A detailed summary of each validation day can be found in Table 4. The average r^2 for the 43 validation days is 0.86, indicating that the slope of boundary elevation is nearly constant. If the boundary does not advance towards the coast and moves around the inland area throughout the day, low r^2 is found such as on June 11. Since the median boundary elevation is consistently higher than zero for this particular day, the least-square regression would suggest a burn-off time that is days away from the forecast issue time. As a result, the line forecast acts like a persistent forecast with only a slight increase in k_t for the day.

To verify that morning k_t exponentially increases to clear sky when the clouds dissipate, the exponential function with coefficients in Table 1 is applied to SolarAnywhere data during June and August 2016. Cloud dissipation time is defined as the first time after sunrise when SolarAnywhere k_t is greater than 0.8. The average of the fitted exponential line is shown in Figure 9, and the hourly k_t MAE is tabulated in Table 5. Note that this analysis is not a forecast since cloud dissipation time is known. Smaller k_t MAE are found at inland stations, while stations in the immediate coast have larger errors (e.g. Solana Beach, San Francisco, and Monterey). The larger errors are due to ambiguous cloud dissipation time or clouds persisting for the whole day. For example, k_t decreases after the first clear point at San Francisco in Figure 9b, and the fitted exponential function is unable to capture any decreasing trend. Similar issues occur in Monterey. All inland stations have hourly k_t MAE less than 0.1, with Lake Wohlford and

Saratoga having the minimum MAE at 0.03. Overall, the exponentially fitted curve are representative for most validation stations.

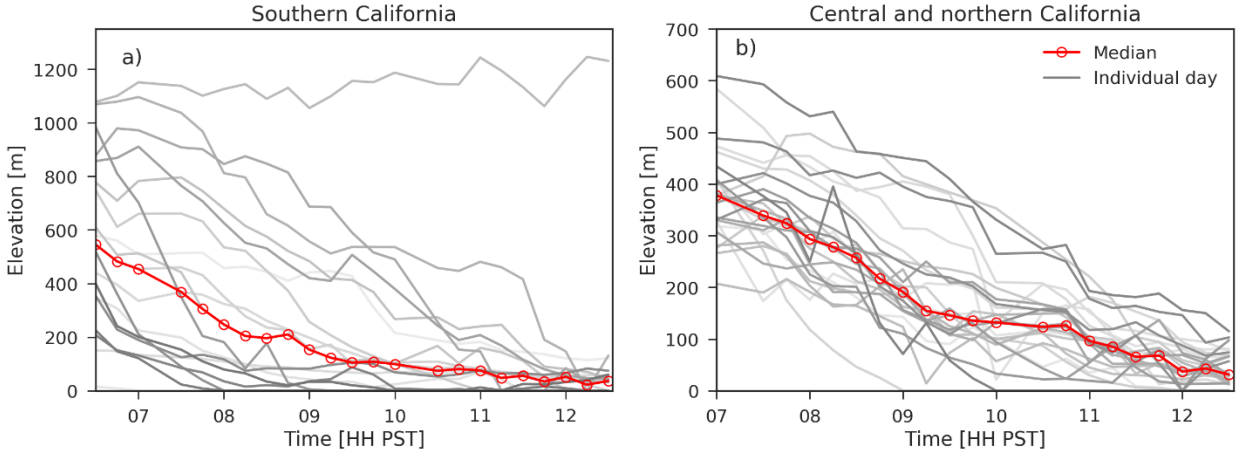

Figure 8. Time series of median cloud edge elevation for 19 days from June, 2016 in a) and 25 days from August, 2016 in b). The median edge elevation is shown in red The cloud edge is detected using GOES data, and the median elevation is obtained from GEBCO.

Table 4
Coefficient of determination for the linear least-square regression through the Sc boundary elevation between 0630 for southern California or 0700 for central and northern California and 1230 PST (or until the land is clear, whichever is earlier). Note that June 2016 is for southern California and August 2016 is for central and northern California.

Date	r^2	Date	r^2	Date	r^2	Date	r^2	Date	R- r^2
1-Jun	0.93	12-Jun	0.91	1-Aug	0.93	11-Aug	0.91	24-Aug	0.83
2-Jun	1.00	13-Jun	0.87	2-Aug	0.88	12-Aug	0.95	25-Aug	0.94
3-Jun	0.69	14-Jun	0.97	3-Aug	0.62	13-Aug	0.76	26-Aug	0.97
4-Jun	0.83	15-Jun	0.90	4-Aug	0.95	14-Aug	0.88	27-Aug	0.98
5-Jun	0.93	23-Jun	0.94	5-Aug	0.97	15-Aug	0.93	28-Aug	0.86
6-Jun	0.88	24-Jun	0.51	6-Aug	0.92	16-Aug	0.92	Average	0.86
7-Jun	0.95	25-Jun	0.59	7-Aug	0.95	17-Aug	0.86		
8-Jun	0.75	29-Jun	0.97	8-Aug	0.98	20-Aug	0.97		
9-Jun	0.96	30-Jun	0.80	9-Aug	0.87	21-Aug	0.89		
11-Jun	0.30			10-Aug	0.94	23-Aug	0.77		

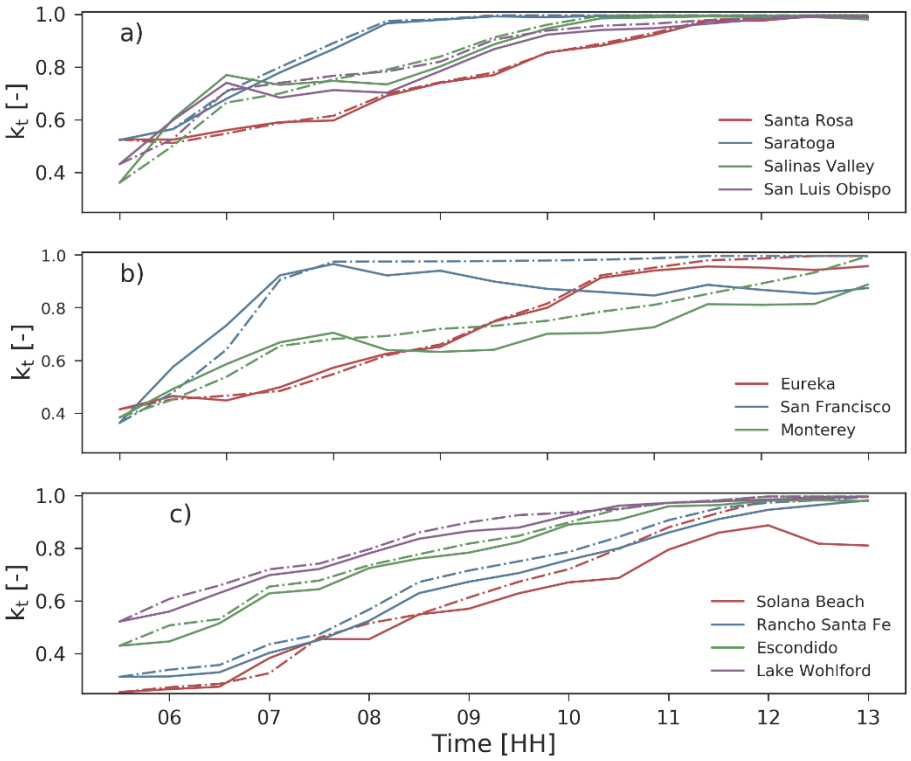

344

Figure 9. Time series of 30-minute instantaneous k_t from SolarAnywhere averaged over all days with known valid cloud dissipation time (i.e. k_t is greater than 0.8). Depending on the station, there are approximately 25 days for (a) and (b) and 19 days for (c); days where k_t never exceeds 0.8 are removed. Solid lines are actual SolarAnywhere averages, and dashed lines are the averaged exponential fits using the coefficients in Table 1. Note that these are hindcasts with known dissipation time to illustrate the exponential fit function. A breakdown of the number of days when clouds did not dissipate is shown in Table 6.

Table 5. Hourly MAE k_t for the exponentially fitted k_t against actual SolarAnywhere k_t data at all validation stations. The fitted k_t is generated with known dissipation time as the first point where SolarAnywhere kt > 0.8.

Station	MAE k_t [-]
Solana Beach	0.13
Rancho Santa Fe	0.06
Escondido	0.04
Lake Wohlford	0.04
Santa Rosa	0.01
Saratoga	0.02
Salinas Valley	0.06
San Luis Obispo	0.06
Eureka	0.04
San Francisco	0.17
Monterey	0.12

Table 6. Number of days when clouds did not dissipate (i.e., persisting days) in southern California in June 2016 and central and northern California in August 2016.

Station	Persisting days [-]	Number of days considered in Figure 9 [-]
Solana Beach	6	19
Rancho Santa Fe	1	19
Escondido	1	19
Lake Wohlford	1	19
Santa Rosa	0	25
Saratoga	0	25
Salinas Valley	0	25
San Luis Obispo	0	25
Eureka	2	25
San Francisco	3	25
Monterey	7	25

4.2 Validation against satellite observations

4.2.1 Southern California

Time series of hourly-averaged GHI from June 5 to 15, 2016 are shown in Figure 10 for forecasts issued from 0700 to 1000 PST. Forecasts issued after 1100 PST are not of interest as clouds have already dissipated on most days and the line forecast would coincide with persistence forecast with a clear sky index of 1. SolarAnywhere GHI shows that Sc clouds tend to stay longer at the coastal site where land elevation is lower. This is consistent with the assumption that Sc eastern boundary moves towards the coast during the day, and the average land elevation of the boundary decreases.

MBE, MAE, and FS are shown in Figure 11. The line forecast consistently performs better than satellite CMV and persistence for all forecast horizon and forecast issue times at Rancho Santa Fe, Escondido, and Lake Wohlford. For Solana Beach, the line forecast is superior to persistence forecast but slightly worse than satellite CMV. The line forecast has the lowest forecast skill for forecast issued at 0700 PST. This is likely because only three visible GOES images are available at the time of the forecast issuance. In addition, the dissipation often happens several hours after sunrise as seen in Table 2 and Table 3, making it difficult to forecast the burn-off time several hours ahead. With later forecast issue times, more images are available and the prediction of burn-off time becomes more accurate. Persistence forecasts have the worst error statistics since Sc clouds are present at the forecast issue time, fixing the clear sky index at the forecast issue time results in under-prediction of irradiance. While satellite CMV forecasts out-perform persistence at all four sites, CMV forecasts under-predict the irradiance. Since Sc clouds do not follow the direction of the synoptic winds, the assumption of CMV breaks down and results in a cloudy bias.

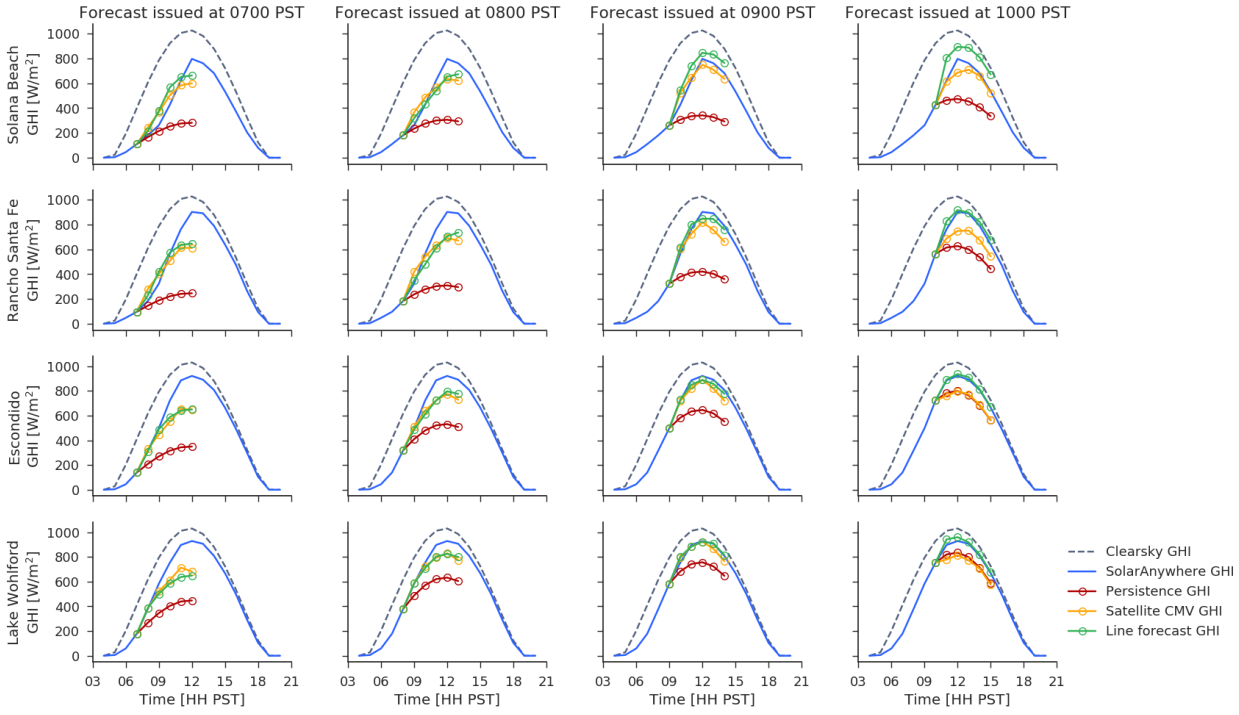

Figure 10: Hourly average of forecasted and satellite observed GHI for all days at Solana Beach, Rancho Santa Fe, Escondido, and Lake Wohlford. Each column represents a different forecast issue time. Note that each circle indicates the irradiance instantaneously at the hour, with the first circle corresponding to the real-time measured data, the second circle being the 1-hour ahead forecast, and the sixth circle being the 5-hour ahead forecast.

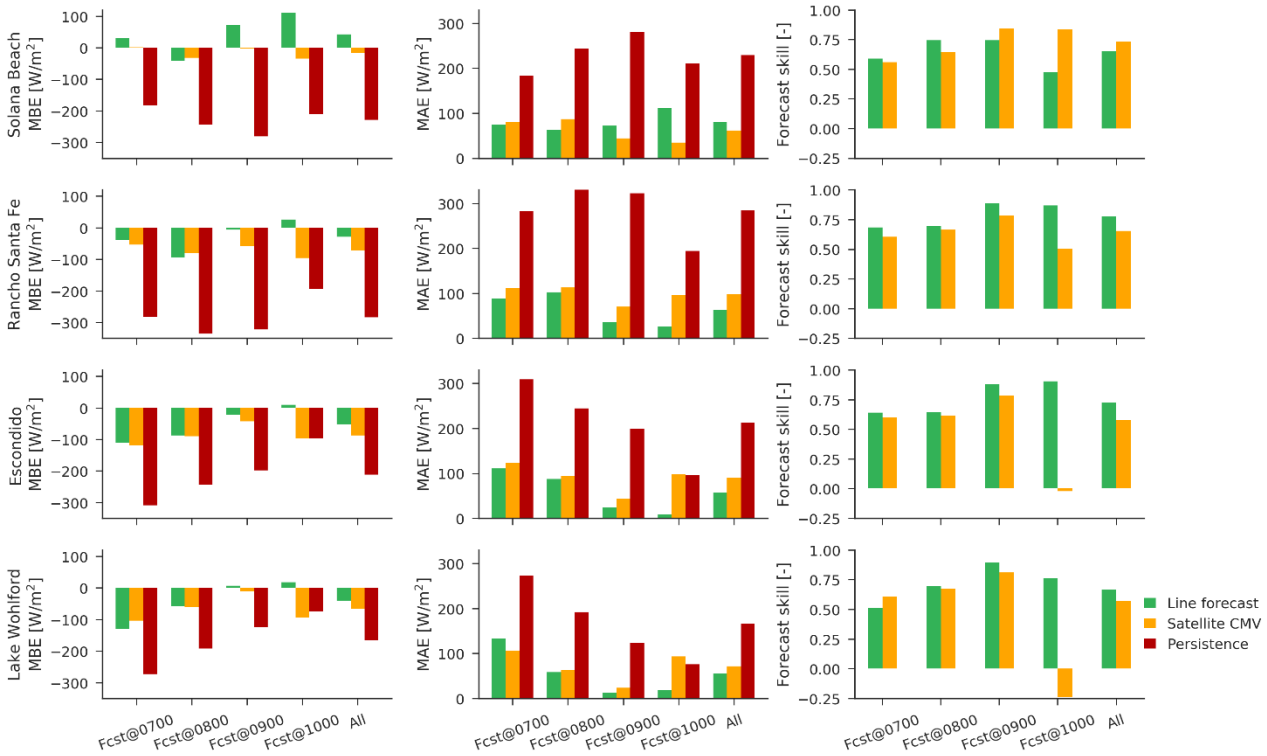

Figure 11: Averaged MBE, MAE, and FS for forecast horizons between 1 to 5-hour ahead for all 19 days at Solana Beach, Rancho Santa Fe, Escondido, and Lake Wohlford.

The coastal topography of San Diego is predominantly north-south oriented, with increasing land elevation from the coast to inland. This simple topographic elevation distribution favors line forecasts because it provides for more consistent meteorological conditions across the forecast domain. For example, (i) absorbed surface irradiance and resulting heating rates are similar due to consistent surface type, (ii) advection is similar due to homogeneous pressure gradients and surface roughness, (iii) microscale meteorological distortions such as local slope flows are avoided, (iv) a straight cloud edge provides for more consistent cloud edge erosion as detailed in the next paragraph. This consistency supports the line forecast assumptions of homogeneous land elevation at the cloud edge and homogeneous rate of change of land elevation at the cloud edge.

Horizontal entrainment of dry air at the cloud edge also plays an important role in the westward movement of the edge. Crosbie et al. (2016) found that the horizontal entrainment at the interface between clear skies and the cloud edge produces evaporatively cooled downdrafts and accelerates the erosion of the cloud edge. In southern California, the cloud edge is relatively straight (north-south) because of the distribution of land elevation. Therefore, horizontal entrainment does not produce as much inhomogeneous mixing as would be the case if the cloud edge was curved and the clear region was not just on one side of the edge. Because of relatively homogeneous lateral mixing and dominant Sc dissipation due to solar heating, the line forecast exhibits significant error reductions compared to persistence and satellite CMV forecasts in southern California.

4.2.2 Central and northern California

The time series of hourly-averaged GHI from the 25 valid days in August 2016 is shown in Figure 12.

MBE, MAE, and FS are shown in Figure 13. The line forecast performs better than persistence forecast at 5 out of 7 sites, and the number drops to 4 when compared to satellite CMV forecast. Unlike the four sites in southern California (Figure 10), more complex terrain makes forecasting the dissipation time of Sc clouds using the line forecast method difficult likely because of cold ocean advection and inhomogeneous horizontal entrainment between the clear and cloudy edge. For Santa Rosa, Saratoga, Salinas Valley, and San Luis Obispo, the line forecast exhibits a similar FS as for the sites in southern California, outperforming the persistence and CMV forecasts over all forecast horizon and forecast issue times. Since these four sites are located away from the immediate coast, solar heating is likely the dominant factor that controls the burn-off time.

SolarAnywhere GHI in Figure 9 indicates that Sc clouds often persist for the whole day at San Francisco and Monterey. Among the four sites in central and northern California where Sc clouds dissipate before noon, it can be seen from the area between SolarAnywhere GHI and clear sky GHI curve (Figure 12) that Saratoga is the least cloudy station. Saratoga also has the highest land elevation among these four sites. Stations in the immediate coast have larger errors (e.g. San Francisco, Monterey) due to ambiguous cloud dissipation time or clouds persisting for the whole day. This phenomenon happens more frequently in the immediate coast as cold advection from the ocean has a greater impact in this region. Ocean advection has smaller impact further inland as the coastal land acts as a barrier for the advection. In some cases, mountain ranges act as a coastal land barrier between the ocean and the station, making it very difficult for clouds to come back after the initial dissipation. For example, the Santa Cruz mountains are located immediately to the west of Saratoga. As a result, it is unusual for ocean advection to have a strong impact at Saratoga, and clear sky is expected after the initial burn-off of Sc cloud deck. Wind direction and coastline orientation also influence whether clouds would come back. The line forecast is expected to perform better at stations outside of the immediate coast as good agreements between fitted k_t and dissipation time are found in Figure 9. In practice, the performance of the line forecast depends on the accuracy of forecasted cloud dissipation time. Figure 9 indicates the best-case scenario of the line forecast (i.e. with known cloud dissipation time).

In complex terrain, many different factors also control the dissipation time. Torregrosa et al. (2016) found that besides land elevation, terrain features placement relative to wind direction and length of terrain feature are important factors controlling Sc cloud coverage. For example, low-lying gaps at Salinas Valley promote inland incursions of Sc clouds. Leeward coastlines (SW-S) are less cloudy than windward (W-NW) coastlines. This is the reason Eureka is cloudier than a station to the south where the coastline changes direction from NW to SW (e.g. Mendocino, located about 150 km south of Eureka) even if both locations have the same land elevation. While taking the median land elevation of the boundary would have falsely flagged places like Mendocino as cloudy, the way the line forecast predicts future k_t automatically corrects these points to clear. However, the line forecast is unable to correct the points that are falsely flagged as clear. This is evident in San Francisco and Monterey (Figure 12) where the line forecast over-predicts irradiance. In fact, satellite CMV forecasts perform better than the line forecast and persistence at these two locations. During the morning forecast issue time, the satellite CMV does not detect movement of Sc clouds, and no cloud advection is being forecasted at the coastal stations. This is the reason satellite CMV forecast behaves similarly to persistence, except that the persistence forecast often suffers from using a fixed single k_t at forecast issue time while CMV averages k_t from previous times.

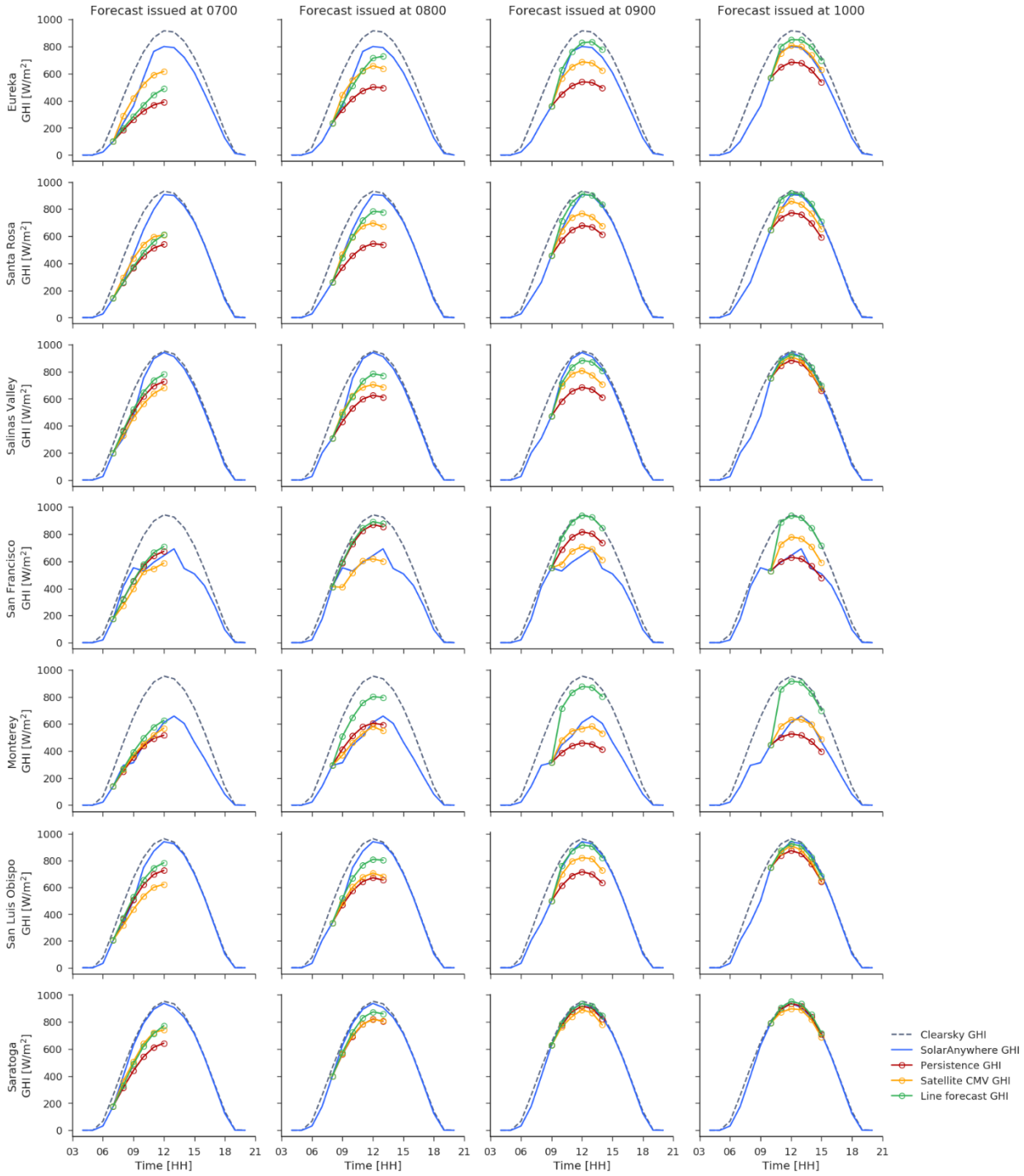

Figure 12: Hourly average of forecasted and satellite observed GHI for August 2016 at seven locations in central and northern California. Each column represents a different forecast issue time.

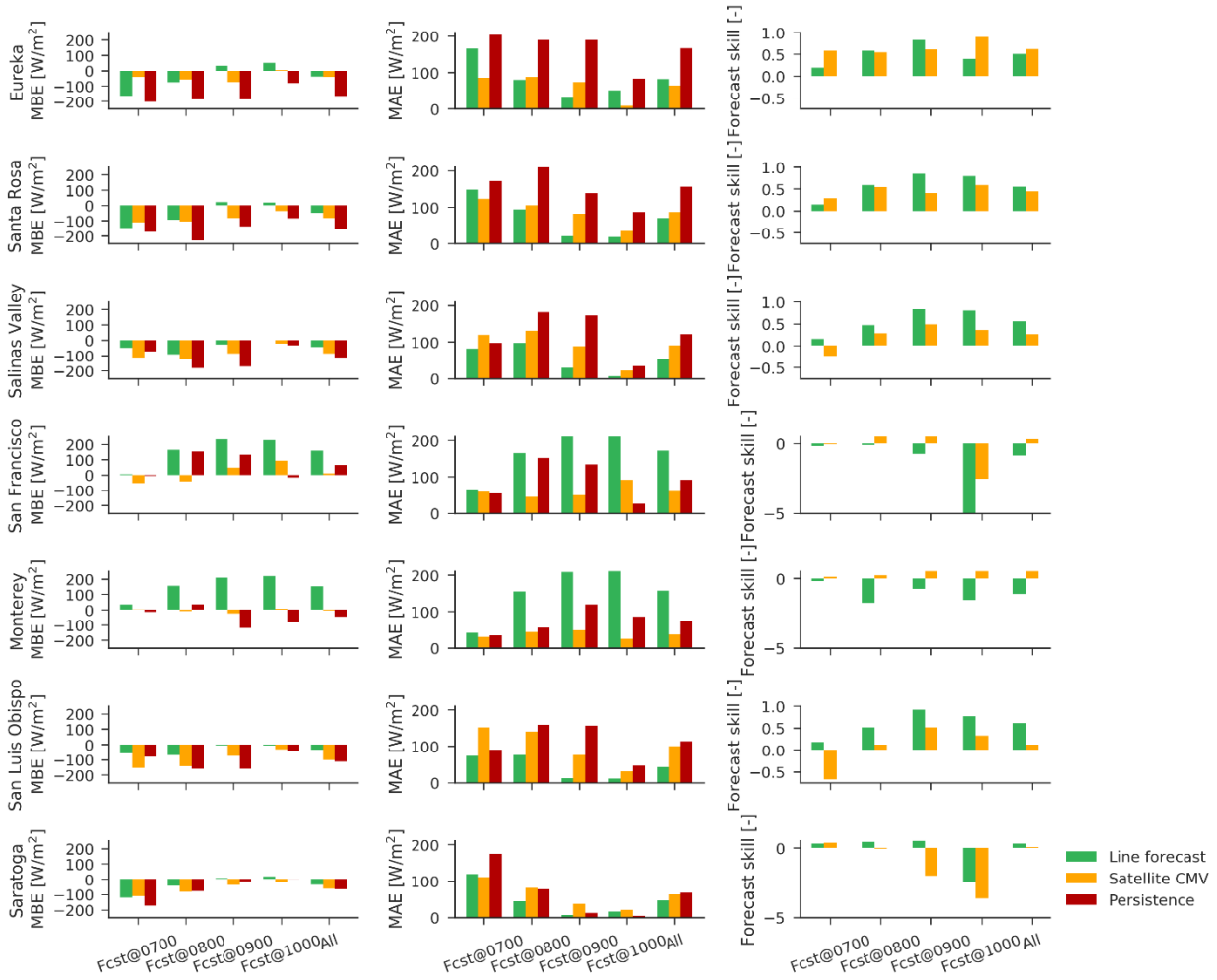

Figure 13: Hourly averaged MBE, MAE, and FS for forecast horizon between 1 to 5-hour ahead from August, 2016 at 7 sites in central and northern California.

4.3 Geographical error distribution

To exhaustively quantify the usefulness of the line forecast, hourly SolarAnywhere GHI data at a horizontal resolution of 2 km is analyzed. Figure 14 is a spatial map of the line forecast FS averaged over all forecasts issued at 0800 PST in southern California, averaged across all forecast horizons, and Figure 15 is for all forecasts issued at 0800 PST in central and northern California. Note that FS has a maximum of 1, and a positive value of FS represents an improvement over persistence forecast.

For southern California, positive FS is found almost everywhere in the domain, making the line forecast a competitive forecast during Sc days. The slightly negative FS around Santa Ana Mountains (33.7^{o}N, 117.5^{o}W) is associated with its high land elevation. Land elevation is often higher than the inversion base height in this area, making it hard for Sc clouds to form (an example can be seen in Figure 1).For central and northern California, positive FS are found in regions slightly away from the coast, while negative FS are found in the immediate coast. Areas of negative FS vary along the coastline. The most negative FS is found along the coast of Monterey Bay— a region with an abundant coverage of low clouds (Clemesha et al., 2016; Torregrosa et al., 2016). Although FS is negative at the San Francisco station chosen in Section 3.4.1, a gradient of FS can be seen near the San Francisco Bay. FS becomes positive about 20 km south of the chosen San Francisco station, including San Francisco International Airport where Sc clouds

often hinder the use of parallel runway due to low visibility. The spatial distribution of FS suggests the use of different forecast systems in different regions. Specific local forecast models based on machine learning and NWP may be more skilled at forecasting Sc cloud lifetime at the immediate coast where clouds tend to persist for the whole day and the line forecast FS are negative. Away from the coast where Sc clouds dissipate during the day and the line forecast FS are positive, the line forecast should be used to forecast GHI.

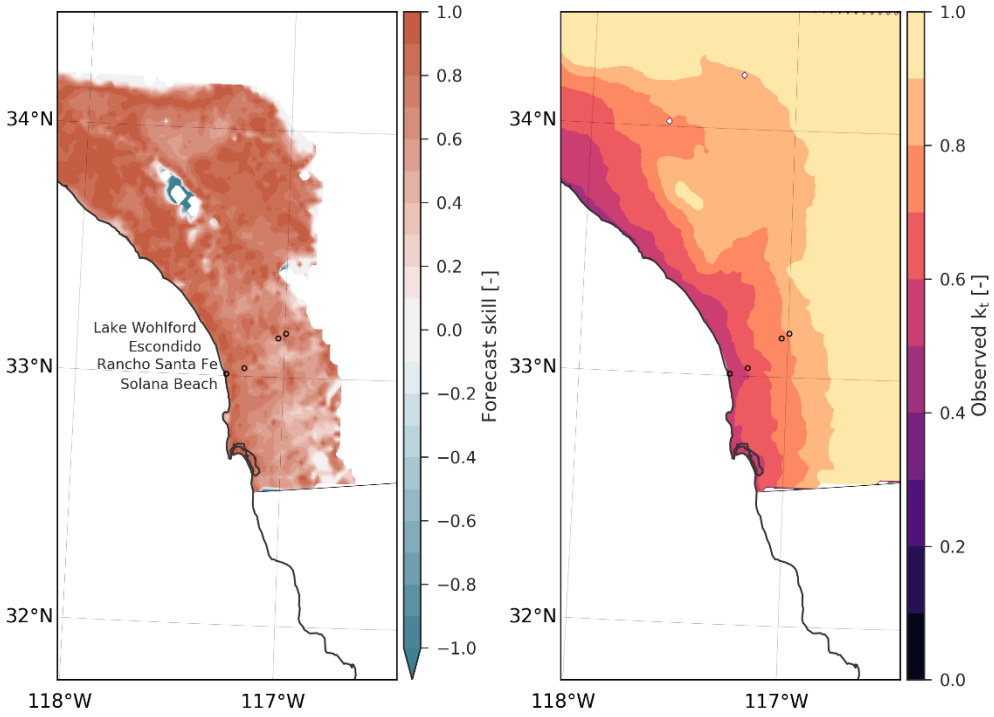

Figure 14. Left: Forecast skill of line forecasts issued at 8 am PST, averaged over 1 to 5-hour ahead for 19 days in June 2016 for southern California. Right: Satellite derived k_t averaged between 7 to 10 PST for 19 days in June 2016.

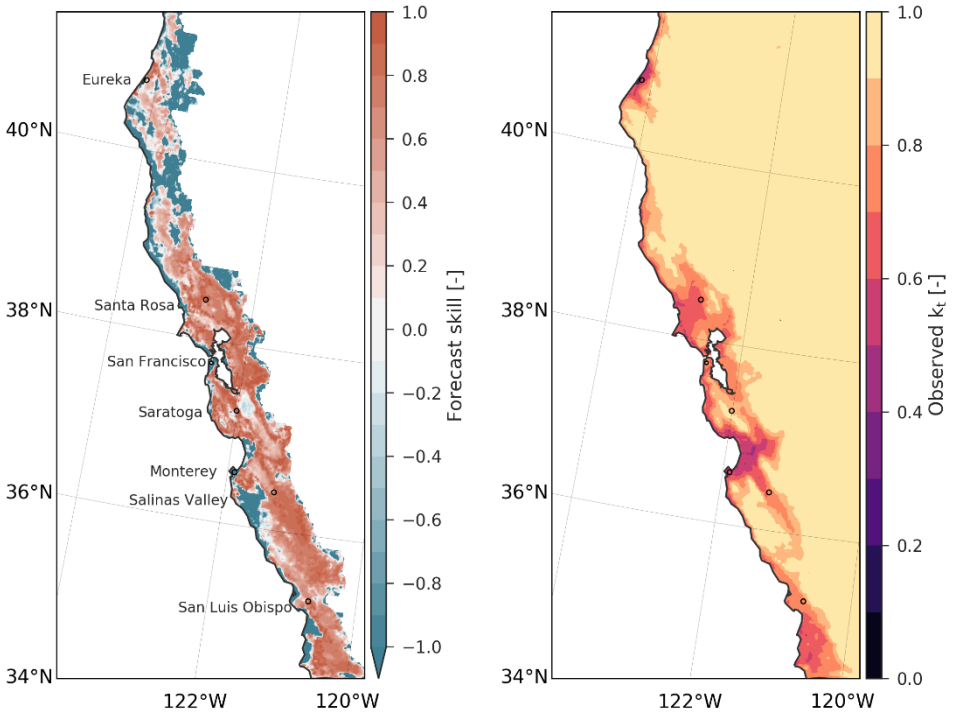

Figure 15. Forecast skill of line forecasts issued at 8 PST, averaged over 1 to 5-hour ahead for 25 days in August 2016 for central and northern California. Right: Satellite derived k_t averaged between 7 to 10 PST for 25 days in August 2016.

5. Conclusions

A Sc line forecast using GOES images is proposed and implemented in coastal California to improve the prediction of cloud dissipation time for forecast horizons between 1—5 hours ahead. The land elevation under the inland boundary of Sc clouds is used to track the cloud boundary and extrapolate it forward in time. This method assumes that solar heating is the main factor controlling the dissipation of Sc clouds during the day, and a decrease in median land elevation at the boundary after sunrise is expected. This is because a strong temperature inversion marks the cloud top height, a lower land elevation means a larger mass of air above ground, and more heat is required to become cloud-free. Validation against satellite solar resource data shows that the line forecast consistently outperforms the persistence forecast at 9 out of 11 stations. In addition, the line forecast outperforms satellite CMV forecast at 7 out of 11 stations. Supplementary validation at 2 km spatial resolution using the same satellite solar resource data shows superior performance to persistence forecasts in most places aside from the immediate coast where Sc clouds may persist for the whole day.

Geographically, the line forecast shows higher forecast skills in southern California than central and northern California. The coastal topography likely plays an important role in the discrepancy in forecast skills (e.g. the simple topographic elevation distribution in San Diego favors the line forecast as it has more consistent meteorological conditions across the forecast domain). The lack of forecast skill in the immediate coast and the sharp gradient of dissipation time within a few kilometers of the coast suggest that at the immediate coast local processes are important in determining when the clouds dissipate. While satellite CMV forecast performs the best in the immediate coast, it is unable to predict the days

when the clouds do dissipate. Improved Sc forecasting is important because of its broad applications such as better management of the grid for the utilities and better planning for the aviation industry. Future work will focus on understanding factors controlling whether Sc clouds would dissipate during the day in the immediate coast.

Acknowledgements

We acknowledge (i) funding provided by the California Energy Commission; (ii) Clean Power Research for providing SolarAnywhere (2017) high resolution satellite-derived irradiance data; (iii) San Diego Gas & Electric Company (SDGE) for access to their ground station irradiance measurements; (iv) helpful comments by Monica Zamora, Xiaohui Zhong, and Handa Yang.

References

Akyurek, B.O., Kleissl, J., 2017. Closed-Form Analytic Solution of Cloud Dissipation for a Mixed-Layer Model. J. Atmos. Sci. 74, 2525–2556. doi:10.1175/JAS-D-16-0303.1

Arbizu-Barrena, C., Ruiz-Arias, J.A., Rodríguez-Benítez, F.J., Pozo-Vázquez, D., Tovar-Pescador, J., 2017. Short-term solar radiation forecasting by advecting and diffusing MSG cloud index. Sol. Energy 155, 1092–1103. doi:10.1016/j.solener.2017.07.045

Beer, C.G.P., Leopold, L.B., 1947. Meteorological factors influencing air pollution in the Los Angeles area. Trans. Am. Geophys. Union 28, 173. doi:10.1029/TR028i002p00173

Chow, C.W., Urquhart, B., Lave, M., Dominguez, A., Kleissl, J., Shields, J., Washom, B., 2011. Intra-hour forecasting with a total sky imager at the UC San Diego solar energy testbed. Sol. Energy 85, 2881–2893. doi:10.1016/j.solener.2011.08.025

CIMIS, n.d. Sensor Specs [WWW Document]. URL http://wwwcimis.water.ca.gov/Stations.aspx (accessed 12.7.17).

Clemesha, R.E.S., Gershunov, A., Iacobellis, S.F., Williams, A.P., Cayan, D.R., 2016. The northward March of summer low cloudiness along the California coast. Geophys. Res. Lett. 43, 1287–1295. doi:10.1002/2015GL067081

Coimbra, C.F.M., Kleissl, J., Marquez, R., 2013. Overview of Solar-Forecasting Methods and a Metric for Accuracy Evaluation, in: Kleissl, J. (Ed.), Solar Energy Forecasting and Resource Assessment. pp. 171–194. doi:10.1016/B978-0-12-397177-7.00008-5

Crosbie, E., Wang, Z., Sorooshian, A., Chuang, P.Y., Craven, J.S., Coggon, M.M., Brunke, M., Zeng, X., Jonsson, H., Woods, R.K., Flagan, R.C., Seinfeld, J.H., 2016. Stratocumulus Cloud Clearings and Notable Thermodynamic and Aerosol Contrasts across the Clear–Cloudy Interface. J. Atmos. Sci. 73, 1083–1099. doi:10.1175/JAS-D-15-0137.1

Denholm, P., Clark, K., O'Connell, M., 2016. On the Path to SunShot. Emerging Issues and Challenges in Integrating High Levels of Solar into the Electrical Generation and Transmission System. Golden, CO (United States). doi:10.2172/1253978

GEBCO, 2017. General Bathymetric Chart of the Oceans [WWW Document]. URL http://www.gebco.net/data_and_products/gridded_bathymetry_data/ (accessed 10.18.16).

Ghonima, M.S., Heus, T., Norris, J.R., Kleissl, J., 2016. Factors Controlling Stratocumulus Cloud Lifetime over Coastal Land. J. Atmos. Sci. 73, 2961–2983. doi:10.1175/JAS-D-15-0228.1

526 Hahn, C., Warren, S., 2007. A GRIDDED CLIMATOLOGY OF CLOUDS OVER LAND (1971–96) AND OCEAN
527 (1954–97) FROM SURFACE OBSERVATIONS WORLDWIDE. Oak Ridge National Laboratory, Carbon
528 Dioxide Information Analysis Center. doi:10.3334/CDIAC/cli.ndp026e

529 Hartmann, D.L., Ockert-Bell, M.E., Michelsen, M.L., 1992. The Effect of Cloud Type on Earth's Energy
530 Balance: Global Analysis. J. Clim. 5, 1281–1304. doi:10.1175/1520-
531 0442(1992)005<1281:TEOCTO>2.0.CO;2

532 Huang, H., Xu, J., Peng, Z., Yoo, S., Yu, D., Huang, D., Qin, H., 2013. Cloud motion estimation for short
533 term solar irradiation prediction. 2013 IEEE Int. Conf. Smart Grid Commun. SmartGridComm 2013
534 696–701. doi:10.1109/SmartGridComm.2013.6688040

535 Iacobellis, S.F., Cayan, D.R., 2013. The variability of California summertime marine stratus: Impacts on
536 surface air temperatures. J. Geophys. Res. Atmos. 118, 9105–9122. doi:10.1002/jgrd.50652

537 Jamaly, M., Kleissl, J., 2012. Validation of SolarAnywhere Enhanced Resolution Irradiation in California.
538 Intern. Rep.

539 Jimenez, P.A., Hacker, J.P., Dudhia, J., Haupt, S.E., Ruiz-Arias, J.A., Gueymard, C.A., Thompson, G.,
540 Eidhammer, T., Deng, A., 2016. WRF-SOLAR: Description and clear-sky assessment of an augmented
541 NWP model for solar power prediction. Bull. Am. Meteorol. Soc. 97, 1249–1264.
542 doi:10.1175/BAMS-D-14-00279.1

543 Johnstone, J.A., Dawson, T.E., 2010. Climatic context and ecological implications of summer fog decline in
544 the coast redwood region. Proc. Natl. Acad. Sci. U. S. A. 107, 4533–8.
545 doi:10.1073/pnas.0915062107

546 Kankiewicz, A., Dise, J., Wu, E., Perez, R., 2014. Solar 2014: Reducing Solar Project Uncertainty With an
547 Optimized Resource Assessment Tuning Methodology. 2014 Am. Sol. Energy Soc. Annu. Conf. 1–6.

548 Klein, S.A., Hartmann, D.L., 1993. The seasonal cycle of low stratiform clouds. J. Clim. doi:10.1175/1520-
549 0442(1993)006<1587:TSCOLS>2.0.CO;2

550 Köhler, C., Steiner, A., Saint-Drenan, Y.-M., Ernst, D., Bergmann-Dick, A., Zirkelbach, M., Ben Bouallègue,
551 Z., Metzinger, I., Ritter, B., 2017. Critical weather situations for renewable energies – Part B: Low
552 stratus risk for solar power. Renew. Energy 101, 794–803. doi:10.1016/j.renene.2016.09.002

553 Lara-Fanego, V., Ruiz-Arias, J.A., Pozo-Vázquez, D., Santos-Alamillos, F.J., Tovar-Pescador, J., 2012.
554 Evaluation of the WRF model solar irradiance forecasts in Andalusia (southern Spain). Sol. Energy
555 86, 2200–2217. doi:10.1016/j.solener.2011.02.014

556 Lee, J.A., Haupt, S.E., Jiménez, P.A., Rogers, M.A., Miller, S.D., McCandless, T.C., 2017. Solar irradiance
557 nowcasting case studies near sacramento. J. Appl. Meteorol. Climatol. 56, 85–108.
558 doi:10.1175/JAMC-D-16-0183.1

559 Mathiesen, P., Collier, C., Kleissl, J., 2013. A high-resolution, cloud-assimilating numerical weather
560 prediction model for solar irradiance forecasting. Sol. Energy 92, 47–61.
561 doi:10.1016/j.solener.2013.02.018

562 Mathiesen, P., Kleissl, J., 2011. Evaluation of numerical weather prediction for intra-day solar forecasting
563 in the continental United States. Sol. Energy 85, 967–977. doi:10.1016/j.solener.2011.02.013

564 NESDIS, 2017. GOES Imager Calibration [WWW Document]. URL
565 https://www.star.nesdis.noaa.gov/smcd/spb/fwu/homepage/GOES_Imager.php (accessed 7.17.17).

Peng, Z., Yu, D., Huang, D., Heiser, J., Yoo, S., Kalb, P., 2015. 3D cloud detection and tracking system for solar forecast using multiple sky imagers. Sol. Energy 118, 496–519. doi:10.1016/j.solener.2015.05.037

Perez, R., Ineichen, P., Moore, K., Kmiecik, M., Chain, C., George, R., Vignola, F., 2002. A new operational model for satellite-derived irradiances: description and validation. Sol. Energy 73, 307–317. doi:10.1016/S0038-092X(02)00122-6

Perez, R., Kivalov, S., Schlemmer, J., Hemker, K., Renné, D., Hoff, T.E., 2010. Validation of short and medium term operational solar radiation forecasts in the US. Sol. Energy 84, 2161–2172. doi:10.1016/j.solener.2010.08.014

Rastogi, B., Williams, A.P., Fischer, D.T., Iacobellis, S.F., McEachern, K., Carvalho, L., Jones, C., Baguskas, S.A., Still, C.J., 2016. Spatial and Temporal Patterns of Cloud Cover and Fog Inundation in Coastal California: Ecological Implications. Earth Interact. 20, 1–19. doi:10.1175/EI-D-15-0033.1

Rienecker, M.M., Suarez, M.J., Gelaro, R., Todling, R., Bacmeister, J., Liu, E., Bosilovich, M.G., Schubert, S.D., Takacs, L., Kim, G.-K., Bloom, S., Chen, J., Collins, D., Conaty, A., da Silva, A., Gu, W., Joiner, J., Koster, R.D., Lucchesi, R., Molod, A., Owens, T., Pawson, S., Pegion, P., Redder, C.R., Reichle, R., Robertson, F.R., Ruddick, A.G., Sienkiewicz, M., Woollen, J., Rienecker, M.M., Suarez, M.J., Gelaro, R., Todling, R., Julio Bacmeister, Liu, E., Bosilovich, M.G., Schubert, S.D., Takacs, L., Kim, G.-K., Bloom, S., Chen, J., Collins, D., Conaty, A., Silva, A. da, Gu, W., Joiner, J., Koster, R.D., Lucchesi, R., Molod, A., Owens, T., Pawson, S., Pegion, P., Redder, C.R., Reichle, R., Robertson, F.R., Ruddick, A.G., Sienkiewicz, M., Woollen, J., 2011. MERRA: NASA's Modern-Era Retrospective Analysis for Research and Applications. J. Clim. 24, 3624–3648. doi:10.1175/JCLI-D-11-00015.1

SolarAnywhere, 2017. Web-Based Service that Provides Hourly, Satellite-Derived Solar Irradiance Data Forecasted 7 Days Ahead and Archival Data Back to January 1, 1998. [WWW Document]. URL https://www.solaranywhere.com/products/solaranywhere-data/ (accessed 7.10.17).

Torregrosa, A., Combs, C., Peters, J., 2016. GOES-derived fog and low cloud indices for coastal north and central California ecological analyses. Earth Sp. Sci. 3, 46–67. doi:10.1002/2014EA000014.Received

Weinreb, M., Han, D., 2011. Conversion of GVAR Infrared Data to Scene Radiance or Temperature [WWW Document]. URL http://www.ospo.noaa.gov/Operations/GOES/calibration/gvar-conversion.html (accessed 7.10.17).

Williams, A.P., Schwartz, R.E., Iacobellis, S., Seager, R., Cook, B.I., Still, C.J., Husak, G., Michaelsen, J., 2015. Urbanization causes increased cloud base height and decreased fog in coastal Southern California. Geophys. Res. Lett. 42, 1527–1536. doi:10.1002/2015GL063266

Wood, R., 2012. Stratocumulus Clouds. Mon. Weather Rev. 140, 2373–2423. doi:10.1175/MWR-D-11-00121.1

Yang, H., Kleissl, J., 2016. Preprocessing WRF initial conditions for coastal stratocumulus forecasting. Sol. Energy 133, 180–193. doi:10.1016/j.solener.2016.04.003

Yang, H., Kurtz, B., Nguyen, D., Urquhart, B., Chow, C.W., Ghonima, M., Kleissl, J., 2014. Solar irradiance forecasting using a ground-based sky imager developed at UC San Diego. Sol. Energy 103, 502–524. doi:10.1016/j.solener.2014.02.044

Zhong, X., Sahu, D.K., Kleissl, J., 2017. WRF inversion base height ensembles for simulating marine boundary layer stratocumulus. Sol. Energy 146, 50–64. doi:10.1016/j.solener.2017.02.021